Advances in Science and Technology Research Journal

Advances in Science and Technology Research Journal, 2026, 20(6), 403–421
https://doi.org/10.12913/22998624/215594
ISSN 2299-8624, License CC-BY 4.0

Received: 2025.11.19
Accepted: 2026.04.15
Published: 2026.05.01

Wire arc additive manufacturing of 5356 aluminium alloy: Processes, properties and performance

Arnold Mauduit[1*], Lauriane Guilmois[1], Sébastien Pillot[1],
Nicolas Bachelard[1], Quentin Lorinet[1]

[1] Centre Technique des Industries Mécaniques, 52 Avenue Félix Louat, 60300 Senlis, France
* Corresponding author's e-mail: arnold.mauduit@cetim.fr

ABSTRACT

This study focuses on wire arc additive manufacturing (WAAM) of 5356 aluminium alloy. An approach combining designs of experiments and artificial neural networks was implemented to identify the optimal parameters for three MIG welding synergies: pulsed MIG, mixed CMT and pulsed MIG, and CMT MIG. The selected optimisation criteria were material health and the visual quality of the samples. The results obtained showed good material integrity for the three configurations studied (in all cases, the porosity rate is below 0.2%). The optimised samples were then subjected to mechanical and microstructural characterisation. The hardness measurements revealed a good level of homogeneity across the wall section and between the different configurations, both in the as-manufactured state and after annealing treatment (1.5 hours at 350 °C). The as built mechanical properties are consistent with the hardness values, with a tensile strength ranging between 250 MPa and 270 MPa. Slight anisotropy is observed between the building direction and the longitudinal direction of the test specimens (a difference of 2% to 4% in Rm and $Rp_{0.2}$). The microstructural analysis of the three configurations revealed similar structures, characterised by columnar grains in the core structure of the beads and fine-grained interfacial zones, contrasting with the structures resulting from conventional welding. This difference is a consequence of an increased concentration of constituents, dispersoids and precipitates in the fine-grained zones, promoting abundant nucleation and selective grain growth. The phases were identified by energy dispersive spectroscopy (EDS). Lastly, a correlation between the microstructure and the mechanical properties was established, highlighting a good match between both aspects.

Keywords: wire arc additive manufacturing, 5356 aluminium alloy, mechanical properties, metallurgical structure.

INTRODUCTION

Additive manufacturing processes based on the use of metal wire can be divided into three categories, depending on the heat source used: Wire electron beam additive manufacturing (WEBAM), wire laser additive manufacturing (WLAM), and wire arc additive manufacturing (WAAM) [1]. The latter is the most common. For these three categories, the general principle remains the same: a layer is formed by melting a metal wire and depositing it on the work area. The formation of a layer by melting this wire is repeated a sufficient number of times to build a part in three dimensions [2, 3]. This technology is a major breakthrough in the production of large-sized metal parts, and it is particularly interesting to produce prototypes, spare parts or small series of components, thanks to its ability to reduce production times and unit costs [4].

In the case of aluminium alloys, WAAM presents specific challenges related to the high thermal conductivity of the material, sometimes combined with residual stresses [5], the formation of porosity [6] and hot cracking susceptibility [5]. However, it is the most widely used additive manufacturing process when working with aluminium alloys. Three welding processes can be used for WAAM of aluminium alloys: GMAW (gas metal arc welding) or MIG (metal inert gas), GTAW (gas tungsten arc welding) or TIG (tungsten inert gas), and PAW (plasma arc welding) [7].

Since many years now, a specific MIG transfer mode has been developed by FRONIUS to improve to address some of the challenges posed by aluminium alloys: the Cold Metal Transfer (CMT) [8]. This method provides less heat input and a stable droplet transfer process assisted by a wire movement during arcing and short-circuit phases [9]. Owing to the low melting point of aluminium alloys, CMT offers particular advantages, such as a low heat input, low distortion, a high welding speed, a high deposition rate and reduced operating costs. For these reasons, CMT is well suited for production with low melting point metals, such as aluminium alloys [9].

There is extensive literature available on 5356 aluminium alloy used with the WAAM process. This is due to the availability of this alloy in welding wire form, as it is widely used in conventional welding for joining 5000 and 6000 series aluminium alloys, and sometimes casting aluminium alloys [10]. Note that the literature mainly focuses on the implementation of 5356 aluminium alloy through different welding strategies (in particular CMT) and addresses the impact of these welding methods in terms of material health (cracking, porosity), mechanical properties and metallurgical structure [11–14]. Porosity is the main internal defect in WAAM-produced aluminium alloy components. Process parameters and deposition strategies applied to 5356 alloy significantly influence this phenomenon, although the observed levels generally remain low, ranging from 0.1% to 0.8% [11, 12]. In addition, the mechanical properties achieved are comparable to those of rolled 5000-series aluminium alloys, with ultimate tensile strengths in the range of 230–275 MPa, but exhibit a marked anisotropy between the welding direction and the build height [11–14]. Finally, residual stresses, while moderate, are not negligible: they range from −75 to +150 MPa along the welding direction and from −75 to +50 MPa in the perpendicular direction, across the build height [13].

This study has the same objectives, allowing to compare and supplement the current literature. However, a different approach was used, relying on our own research and parametric optimisation method, and the analysis was extended to establishing a correlation between the microstructure and the mechanical properties.

MATERIALS AND METHODS

Material and test specimens

Owing to their good operative weldability, Al-Mg type alloys are widely used as filler metals when welding the various aluminium alloys [15]. 5356 aluminium alloy (AWS A 5.10 / ASME II C SFA5.18M ER5356 / NF EN ISO 18273 S Al5356 (AlMg5Cr(A))) is one of those alloys that are the most often used as filler metals, as it features good mechanical strength, excellent corrosion resistance and, of course, good weldability. It contains approximately 5% Mg, with the presence of Cr and Mn. Cr controls grain growth and, in combination with Mn, reduces the tendency of weld beads to crack during the cooling phase [16]. As previously mentioned, this alloy is readily available in spools and was supplied in 1.2-mm diameter wire for all the fabrications of the study.

The test specimens made for the parametric research and for physical and mechanical characterisation are “walls” with dimensions of approximately 150 × 100 × 15 mm (see Figure 1).

The substrate is a 5754 aluminium alloy plate, with the same dimensions for all fabrications, i.e. 450 × 80 × 10 mm.

Manufacturing equipment

The WAAM cell consists of a 6-axis Fanuc ArcMate i120 robot with two dual-axis external positioners and a Fronius TPS/i 600A welding generator (MIG/MAG). In addition, we used a Fronius water-cooled welding torch (Robacta Drive CMT model) and a Fronius wire reel (WF25i REEL model). The AdaOne CAD/CAM and data acquisition / visualisation software (supplied by Adaxis) were also used.

Characterisation methods

The chemical analyses were carried out using several techniques, depending on the type of test specimen and the elements to be analysed. The oxygen (O) content was determined with the IGF-NDIR technique (inert gas fusion – non-dispersive infrared). The carbon (C) content was determined by IR combustion. The sulphur (S) content was determined by GDMS (glow discharge mass spectrometry). The other elements were determined by ICP-OES (inductively-coupled plasma – optical emission spectroscopy) (SPECTRO

Figure 1. Example of "wall" test specimens

ARCOS FHX22 instrument) after dissolution of the "wire" sample, and by spark OES (spark-optical emission spectroscopy) (Ametek Spectrolab instrument) for the solid samples ("wall" test specimens). The measurement uncertainties were calculated with a coverage factor of 2, which corresponds to a confidence interval of 95%.

The porosity measurements were carried out using the Archimedes or double weighing method [17], particularly during the parametric research process. This is the most commonly used method for quickly determining the porosity of parts and test specimens produced by metal additive manufacturing. Porosity measurements by image analysis were also performed on the "wall" test specimens, using an Axio imager M2m optical microscope (Zeiss) [18].

The Brinell (HBW 5/250) hardness measurements were carried out at room temperature using an Emco-Test Duramin 500 hardness tester (in accordance with standard EN ISO 6506-1). At least three measurements were made per test specimen (only the average is presented).

To measure the electrical conductivity of non-magnetic metals (which is the case of aluminium alloys), we relied on the eddy current testing technique. The instrument used was a Fisherscope MMS PC equipped with an ES40 probe, which is itself equipped with a thermocouple. As a result, the Fisherscope instrument can instantly correct the electrical conductivity as a function of the temperature. A frequency of 60 kHz was set to ensure deep penetration into the alloy.

The tensile tests were carried out in accordance with standard ISO 6892-1 (A224) at room temperature, using a MAYES ESM250 tensile testing machine (250 kN) equipped with a MF Mini MFA2 extensometer. The test specimens (cylindrical type with threaded head) were extracted from the "wall" specimens along the vertical direction (height of the walls, referred to as Z) and horizontal direction (length of the walls, referred to as X). The strain rate was constant and set to 6×10^{-3} s^{-1}.

The samples for micrographic examinations were prepared using conventional methods (cutting, resin mounting, polishing, etc.) before examination with a Zeiss Axio Imager M2m optical microscope. Chemical etching for the examinations was performed using Barker's reagent (electrolytic etching).

The samples for scanning electron microscope examination were prepared using conventional methods and examined with a JEOL JSM-IT800 FEG-SEM. This microscope is equipped with an Oxford Ultim Max 100 EDS (energy dispersive x-ray spectroscopy) sensor and an Oxford CMOS Symmetry EBSD (electron back scattering diffraction) camera. The EBSD and EDS maps were produced with the AztecCrystal 2.1 and Aztec 5.1 data analysis software programs, respectively.

The equipment used for the annealing heat treatment (1.5 hours at 350 °C – air cooling) is a Nabertherm forced convection air furnace. This furnace is designed for heat treating aluminium alloys (at temperatures $\leq$ 650 °C) and features excellent temperature homogeneity ($\Delta T \leq 6$ °C).

RESULTS AND DISCUSSION

Parametric research and optimisation

The WAAM process relies on several key parameters (similarly to conventional welding) to ensure that the fabricated parts are made with a high level of quality and precision. The main welding parameters are listed below:

- Wire feed speed (WFS) – this is the speed at which the wire is fed into the welding torch. It is generally between 5 m/min and 8 m/min.
- Travel speed (TS) – corresponds to the speed at which the welding torch moves. Constant speed is crucial to avoid fabrication defects.
- Voltage (U) – this is the voltage applied during the welding process. It has an influence on the stability of the arc and the quality of melting.
- Current (I) – this is the current used during the welding process. It affects the amount of

heat generated and the depth of penetration during welding.

In the literature [19, 20], it is common practice to use the linear welding energy in relation to the heat input to describe the thermal cycles during WAAM. It is defined as follows:

$$E_l = \frac{U\,I}{TS} \tag{1}$$

However, as the energy has an influence on each gram of material deposited [21], it appears more relevant to monitor the mass energy E_m. It is defined as follows:

$$E_m = \frac{U\,I}{TS}\,\frac{1}{\frac{\pi}{4}\,\text{Ø}_{wire}^2\,\rho} \tag{2}$$

where: Ø_{wire} is the diameter of the filler wire – ρ is the density of the 5356 aluminium alloy.

However, since we use only one wire diameter and one alloy, Ø_{wire} and ρ are constant for all fabrications, which amounts to using the linear welding energy as one item of input data for our parametric research, which is carried out using the design of experiments method and an artificial neural network (ANN). In addition to the linear welding energy, the power which is related to the WFS by the welding synergy, and the argon (Ar) content in the Ar-He gas mixture are used as input data for the design of experiments. Three MIG synergies are evaluated: pulsed MIG, mixed CMT and pulsed MIG, and CMT MIG. A Box-Behnken type design of experiments [22] was used to optimise the positioning of the tests in the parametric space. The responses or output data studied are material health (with the void ratio measured by the double weighing method as quantitative data) and the visual quality of the wall (with the "aesthetic" perception rating of the manufactured wall as quantitative data).

Artificial Neural Networks (ANNs) are used to model the relationship between the input parameters (linear welding energy, power, argon content) and the output parameters (visual quality and porosity of the walls). A network with a hidden layer between the input layer and the output layer can approximate any continuous function of $\mathbb{R}^p$ in $[0;1]^n$ [23, 24], making it suitable for handling complex relationships between the input data and the observed responses. ANNs work by:

- Supervised learning – the network learns from known data.
- Retropropagation – errors between expected responses and produced responses are corrected [25].
- Inertial terms, which help to avoid local minima during optimisation.

An overly complex ANN can overfit the training data and thus lose its ability to generalise. To avoid this, a validation dataset and early stopping are used to stop the training process before overfitting occurs and thus improve the generalisation performance of ANNs [26]. Modelling is performed using an ANN with a single hidden layer, with three neurons in that hidden layer. For each welding method, we carried out 18 wall fabrication tests with different parameters. Among these, 15 tests were used to make up the training base, while the remaining 3 tests were used to validate the model. Once the ANNs have been trained, it becomes possible to determine a parametric optimum for each of the abovementioned MIG synergies.

Lastly, one "wall" test specimen was produced with the optimised parameters (determined as previously indicated) per synergy, for the purpose of analysis. In addition, one of the most important parameter in WAAM is the creation of paths which control the movement of the welding torch to fill the 2D layers representing the transverse geometry of a fabricated part or test specimen. For this study, the layers were filled through triangular weaving movements with alternating start and stop between each layer, resulting in a more homogenous distribution of the material [27]; in addition, an interlayer temperature was defined. The next layer only starts when the temperature of the previous layer is between 150 °C and 155 °C; this is achieved using a controlled thermal imaging camera.

Table 1 summarises the optimised configurations for each MIG synergy. Note that configuration No. 3 in conventional or standard CMT features lower linear welding energy than the other two configurations, which have values closer to each other.

Characterisation of optimal parameters

In the remaining part of the study, the three "wall" test specimens are analysed and identified by the name of the configuration (Table 1). The examinations and tests carried out in the rest of the study allowed us to comment and compare the three configurations.

Table 1. Optimised configurations determined through parametric analysis

Configuration	MIG synergy	Parameters	Linear welding energy (E_l) (in J/mm)	Deposition rate (in kg/h)
1	Pulsed MIG	U = 17.5 V I = 117 A WFS = 6.8 m/min TS = 15 mm/s Pure argon gas – 3,67 m^3/s (22 l/min)	136.5	0.58
2	Mixed CMT and pulsed MIG	U = 19.2 V I = 129 A WFS = 7.5 m/min TS = 16.6 mm/s Pure argon gas – 3,67 m^3/s (22 l/min)	149.2	0.58
3	CMT MIG	U = 14.3 V I = 109 A WFS = 7.5 m/min TS = 16.6 mm/s Pure argon gas – 3,67 m^3/s (22 l/min)	93.9	0.60

Note: 99.998% pure argon gas.

Morphological analyses of the walls

Figure 2 illustrates the walls produced in the three optimised configurations.

The optimised walls are well built. However, configuration No. 2 exhibits fairly significant sagging at the start and end of the wall, compared to the other two configurations. Also note the presence of a more pronounced thickness reduction at the base of the wall in configuration No. 3. To provide a more in-depth morphological analysis, we measured some of the dimensional characteristics of the walls (Table 2): wall width, wall height, layer thickness, penetration, etc. For information, layer thickness is determined by means of two methods:

- Weld pool line intercept method described in [28].
- Wall height/number of layers ratio method.

Figure 3 represents the connection between the data in Table 2 above to the linear welding energy. It can be seen that:

- The width (max. and min.) of the walls and the penetration into the substrate increase linearly as the linear welding energy increases.
- The layer thickness decreases as the linear welding energy increases.

Additional heat input causes the weld pool to spread, resulting in greater deposit width and therefore reduced layer thickness. With a higher heat input, it also seems logical that penetration into the substrate should be better. On the other hand, the smaller width at the base of the wall indicates that applying identical parameters throughout the fabrication process is not an ideal solution. This is the consequence of insufficient wetting between the first layer and the substrate, due to the excessively small amount of energy input and the low temperature of the substrate [29]. To overcome this problem, i.e. to achieve better penetration and a wider wall base, it is advisable to use different, more energetic parameters for the first or even the second layer and then return to the defined parameters. Thus, configuration No. 1 or No. 2 may be used for the first two layers, and configuration No. 3 for the rest of the wall. Pre-heating the substrate that has already been installed is also a possibility for improved penetration.

Chemical analyses

Table 3 presents the results of the chemical analyses performed on the wire sample taken directly from a spool and on the three “wall” samples taken from the configurations identified as No. 1, No. 2 and No. 3.

All samples are found to correspond to the aluminium alloy grade 5356. We can consider that there are no changes in the chemical composition for configurations No. 1 and No. 3 compared to the filler wire. This is less true for configuration No. 2: a slight loss of Mg is noted; this can potentially be explained by a more energetic configuration (Table 1), causing the evaporation of the most volatile elements.

Material integrity

Material integrity is characterised by the amount of porosity observed on a micrographic section. The study samples consist of cubic specimens (approximately 15 × 15 × 15 mm) extracted

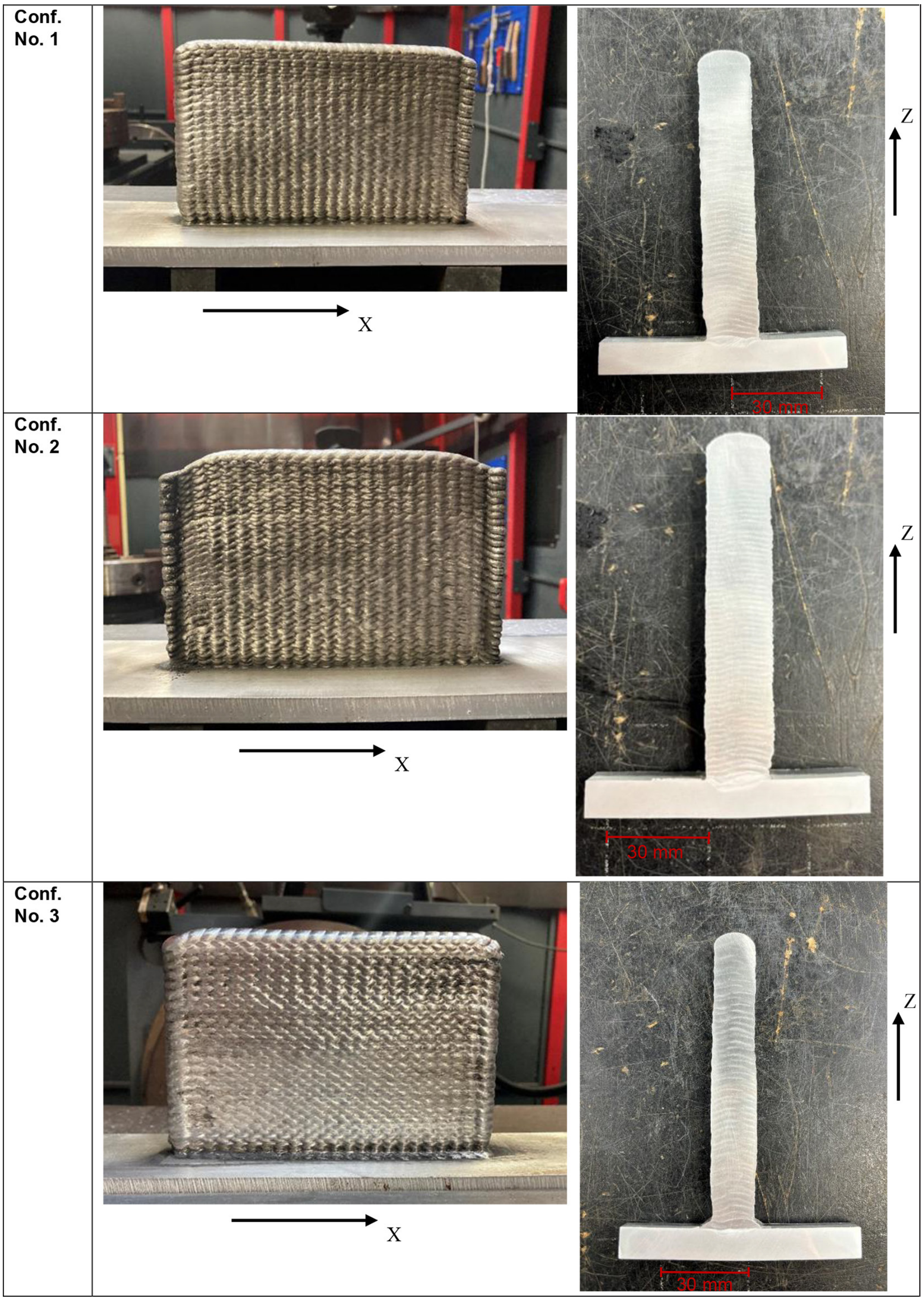

Figure 2. Examinations of the walls fabricated in configurations No. 1, No. 2 and No. 3. Side view and cross-sectional view (macrography)

Table 2. Summary of dimensional data for the walls produced in the three configurations

Dimensional characteristics	Configuration No. 1	Configuration No. 2	Configuration No. 3
Width (in mm)			
Max.	18.5	20.4	15.9
Min.	17.7	18.4	14.8
Base	16.6	17.4	13.4
Average height (in mm)	96.1 (53 layers)	101.5 (62 layers)	99.9 (46 layers)
Penetration (in mm)	2.0	2.9	1.1
Layer thickness (in mm)			
Intercept method	1.7	1.6	2.1
Number of layers method	1.8	1.6	2.2

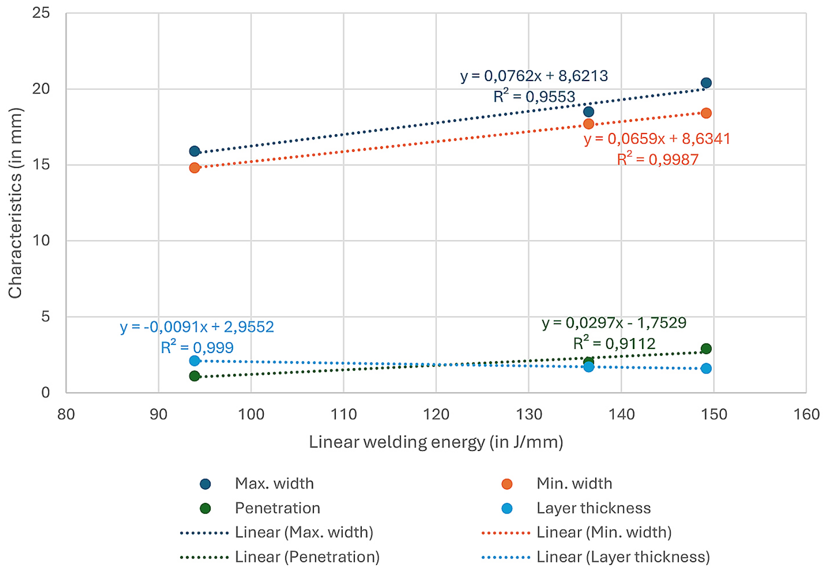

Figure 3. Welding geometric characteristics as a function of the linear welding energy

Table 3. Chemical analyses of the samples studied

Elements	Al 5356 NF EN ISO 18273	Wire	Conf. No. 1	Conf. No. 2	Conf. No. 3
Iron %	≤ 0.40	0.079 ± 0.011	0.086 ± 0.010	0.089 ± 0.011	0.086 ± 0.010
Silicon %	≤ 0.25	0.13 ± 0.01	0.068 ± 0.008	0.066 ± 0.008	0.067 ± 0.008
Copper %	≤ 0.10	≤ 0.004	≤ 0.020	≤ 0.020	≤ 0.020
Zinc %	≤ 0.10	0.008 ± 0.002	≤ 0.015	≤ 0.015	≤ 0.015
Magnesium %	4.5 – 5.5	4.83 ± 0.17	4.80 ± 0.16	4.67 ± 0.15	4.76 ± 0.16
Manganese %	0.05 – 0.20	0.15 ± 0.01	0.14 ± 0.01	0.14 ± 0.01	0.14 ± 0.01
Nickel %	≤ 0.05	≤ 0.005	≤ 0.010	≤ 0.010	≤ 0.010
Chromium %	0.05 – 0.20	0.12 ± 0.01	0.13 ± 0.01	0.13 ± 0.01	0.13 ± 0.01
Titanium %	0.06 - 0.20	0.089 ± 0.004	0.089 ± 0.010	0.087 ± 0.010	0.087 ± 0.010
Lead %	≤ 0.05	≤ 0.005	≤ 0.010	≤ 0.010	≤ 0.010
Tin %	≤ 0.05	≤ 0.020	≤ 0.015	≤ 0.015	≤ 0.015
Vanadium %	≤ 0.05	0.012	0.014 ± 0.004	0.014 ± 0.004	0.014 ± 0.004
Carbon %	-	≤ 0.0010	0.0014	0.0013	0.0013
Sulphur %	-	0.000054	0.000051	0.000046	0.000038
Oxygen %	-	≤ 0.0001	≤ 0.0001	≤ 0.0001	≤ 0.0001

at roughly one-third and two-thirds of the wall height. The reported values (Table 4) represent the mean of observations performed on five fields within a micrographic cross-section obtained from both cubes. The image presented in the right-hand column is chosen arbitrarily among the 2 × 5 observation fields, but it provides a fairly accurate representation of porosity.

In general, the three configurations offer good material integrity with low porosity rates.

All the defects observed are round pores similar to those found during “conventional” welding, with hydrogen being the main cause. At the solid-liquid interface, during the solidification of the fabricated part, the newly created solid phase discharges the dissolved hydrogen into the liquid phase [30]. The hydrogen eventually exceeds the solubility limit in the liquid as a result of its accumulated quantity. The high thermal conductivity of aluminium causes rapid solidification of the weld pool from the outside to the inside, trapping the pores generated by hydrogen. The main source of hydrogen in WAAM of aluminium is the filler wire. Compared to conventional welding, the

Table 4. Observation of porosity on micrographic sections for the three configurations

Configuration	Image porosity	Image (representative)
1	Porosity rate: 0.02% ± 0.01% Equivalent diameter of the largest pore: 27.7 µm	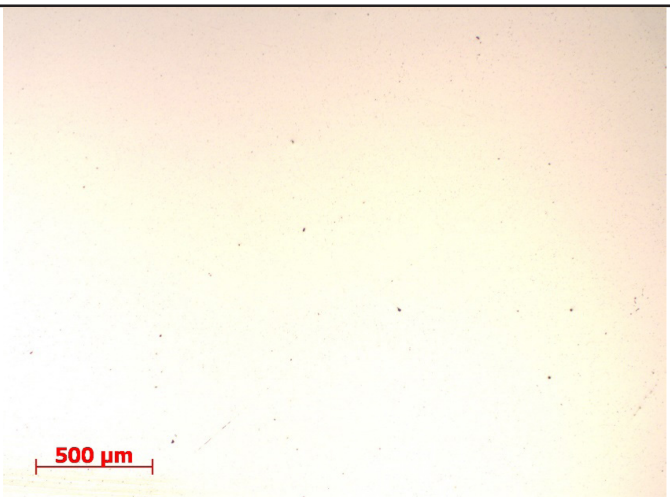
2	Porosity rate: 0.16% ± 0.08% Equivalent diameter of the largest pore: 82.1 µm	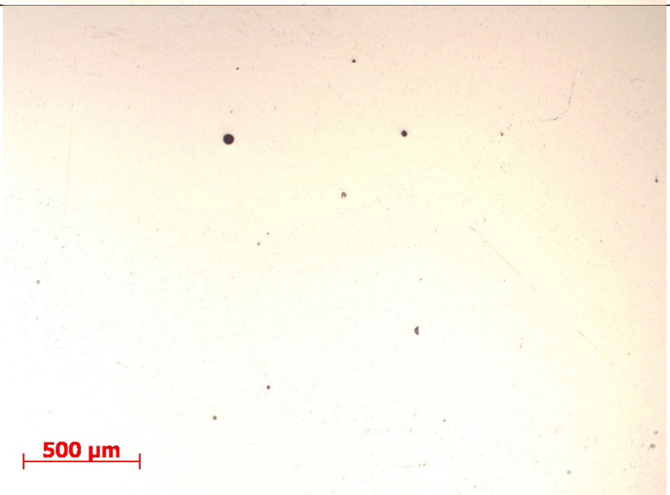
3	Porosity rate: 0.03% ± 0.01% Equivalent diameter of the largest pore: 33.5 µm	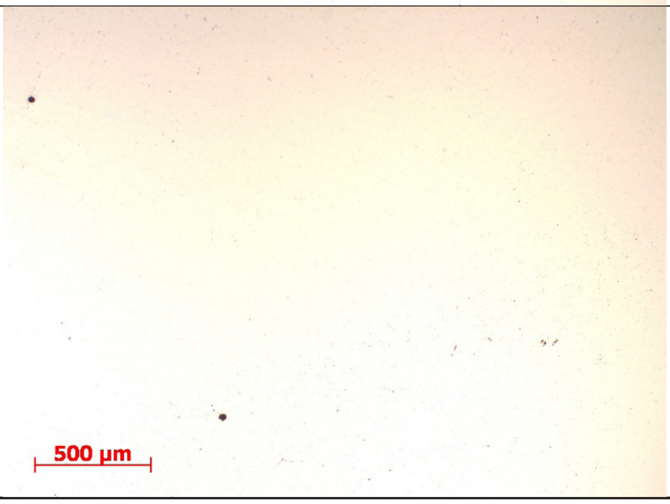

formation of hydrogen pores in aluminium components fabricated by WAAM can be more difficult to control, since the filler wire is introduced into the weld pool in large volumes [31].

We can see that configuration No. 1 is the cleanest, with a very low porosity rate. Conversely, configuration No. 2 appears to have the poorest material integrity. It should be noted that the largest defects are observed in configuration No. 2. Configurations No. 1 and No. 3 exhibit almost equivalent defect sizes. Linear welding energy has a direct impact on the porosity rates of the deposited beads [19]: the energy input needs to be reduced to achieve improved material health. However, configuration No. 2 is the most energetic, which can explain the observations presented in Table 4.

Hardness and electrical conductivity

Figure 4 presents the method and areas for hardness measurement on one section from each configuration studied, in the as built condition.

It should be noted that the HBW hardness values are in line with the mechanical properties presented below. There is little to no difference between the configurations. The hardness values are fairly homogenous across the section (the wall height), for all configurations.

Table 5 presents the results of hardness and electrical conductivity measurements on a cube-shaped test specimen cut from the walls of configurations No. 1, No. 2 and No. 3.

No change is observed in the hardness value after annealing (1.5 hours at 350 °C), regardless of the synergy; this is interesting because the heat treatment allows residual stresses to be removed when necessary, with no impact on the mechanical properties. Electrical conductivity is almost identical for the three configurations, which is indicative of an undoubtedly very similar structural state. No change is observed in electrical conductivity after heat treatment, which confirms that no structural change occurs after heat treatment. In this type of alloy, non-hardening precipitation of Al_3Mg_2 is possible, particularly at grain boundaries, and may be an issue with regard to the corrosion resistance of the alloy. It would be advisable to ascertain this point to complete the study. However, since there is no change noted in electrical conductivity after heat treatment, this may suggest that no "further" precipitation occurs (particularly of Al_3Mg_2).

In conclusion, it seems that there is no change in the structure and no change in precipitation after annealing treatment.

In addition to verifying the resistance to corrosion (particularly intergranular corrosion) of the alloy, the study could be expanded to analyse the impact of the heat treatment on the residual stresses. As a matter of fact, it can be assumed that the level of residual stresses is higher in the as-fabricated state than after the annealing heat treatment.

Mechanical properties

Figure 5 presents the conventional mechanical properties of the different configurations studied, in the as-fabricated state. It emerges that:

- The mechanical properties of the three configurations are fairly similar. Regardless of the configuration and the test direction, the Rm value ranges between 250 MPa and 270 MPa, the $Rp_{0.2}$ value ranges between 110 MPa and 120 MPa, and the elongation value ranges between 22% and 32%. Note that configuration No. 3 exhibits systematically higher Rm and $Rp_{0.2}$ values (by a few MPa) than the other two configurations.
- Slight anisotropy is noted between the X direction and the Z direction. As a matter of fact, the Rm and $Rp_{0.2}$ values are 2% to 4% higher in the X direction. This can be rather easily explained by the "layer-by-layer" or, more precisely, "bead-over-bead" fabrication method, where the Z direction (the building or bead stacking direction) features slightly lower mechanical properties. This phenomenon is observed in many layer-by-layer fabrication processes.

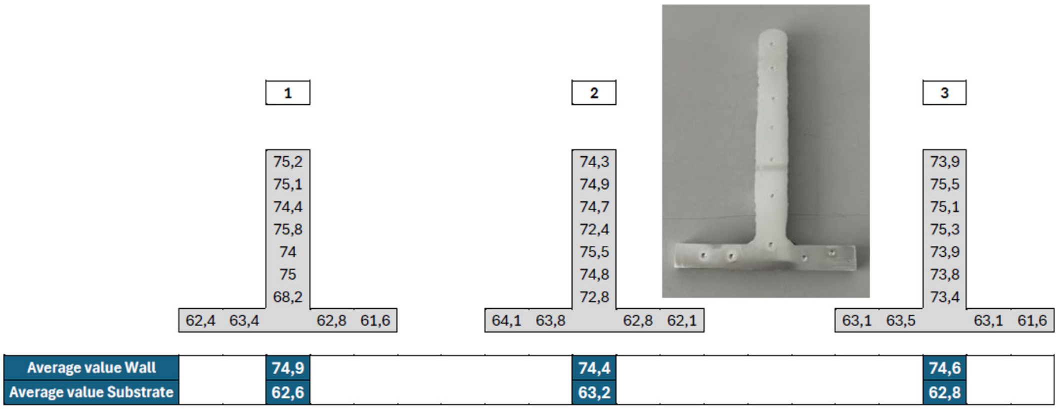

Figure 4. Hardness HBW 5/250 on the three wall sections from the three configurations identified as No. 1, No. 2 and No. 3. As built

Table 5. Hardness HBW 5/250 and electrical conductivity measurements on test specimens sampled from the walls, before and after heat treatment (annealing)

Configuration	Hardness HBW 5/250	Electrical conductivity (MS/m)
1 – As built	74.6 ± 0.5	15.42 ± 0.02
2 – As built	72.3 ± 0.6	15.47 ± 0.02
3 – As built	72.7 ± 1.0	15.46 ± 0.01
1 – Heat treated	73.3 ± 0.8	15.46 ± 0.02
2 – Heat treated	73.8 ± 1.2	15.60 ± 0.02
3 – Heat treated	73.5 ± 1.3	15.47 ± 0.03

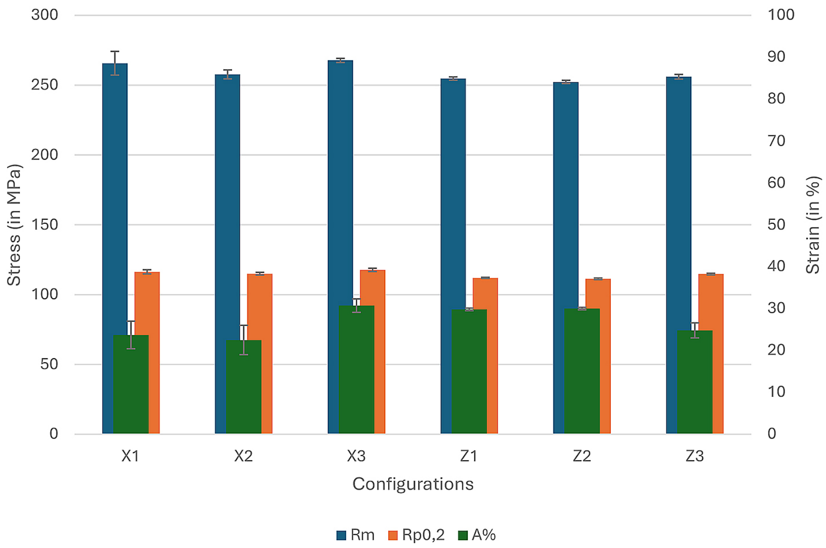

Figure 5. Mechanical properties of configurations No. 1, No. 2 and No. 3 in the X direction (wall length) and the Z direction (wall height). As fabricated

- The mechanical properties obtained in our study in the as built condition are comparable to those reported in the literature on this subject [11–14]. In fact, the Rm value is roughly in the range of 250 MPa to 260 MPa, the $Rp_{0.2}$ value is in the range of 100 MPa to 120 MPa (with the exception of [14], where $Rp_{0.2}$ is rather around 160 MPa to 180 MPa), and the elongation value varies between 15% and 30%. Therefore, our results are rather above average.

The MIG synergy does not seem to significantly affect the mechanical properties.

Figure 6 shows examples of tensile curves for configuration No. 3 (CMT MIG) in the as built condition: one curve in the X direction and one curve in the Z direction. As previously indicated, there is slight anisotropy between the two directions. Instabilities can also be noted on both curves. During the tensile test performed at a constant imposed strain rate, these instabilities are characterised by the appearance of typical stress jumps on the mechanical response curve (Figure 6). These are Portevin – Le Chatelier (PLC) instabilities [32] which are "classically" observed in 5000 series aluminium alloys. 5356 aluminium alloy is no exception. These instabilities are permanent and propagative.

We compared the PLC instabilities for each configuration (No. 1, No. 2 and No. 3) based on two quantitative criteria: the frequency (inverse of periodicity) of the instabilities and the amplitude of the instabilities. Table 6 summarises our observations for two strain values, one at approximately 5% to 7%, and the other one at approximately 15% to 17% in the X direction. In the second part of the table 6, an example of PLC instability measurement (configuration no. 3) is provided: illustrating the period (inverse of the frequency) and the amplitude (in MPa).

For all configurations, a change in the instabilities within the tensile curve itself can be noted: a difference between PLC instabilities at 5% and

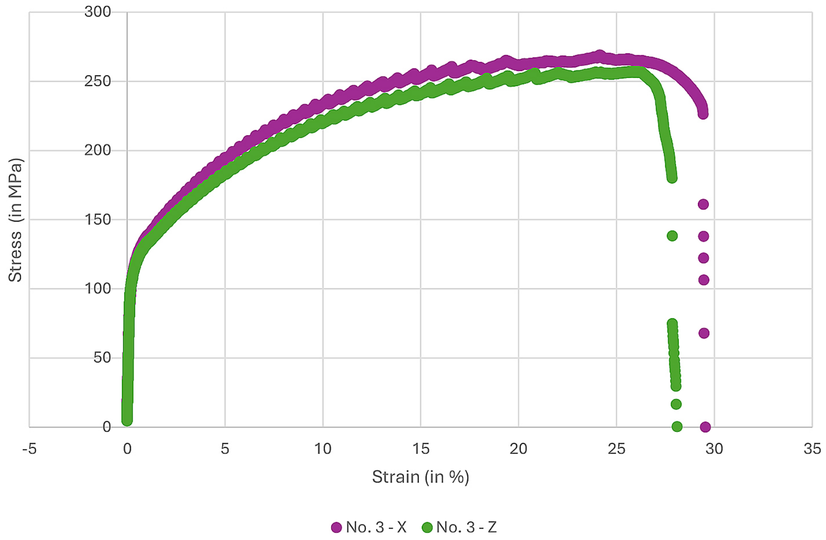

Figure 6. Conventional tensile curves. Configuration No. 3. X and Z directions

at 15% elongation. As a matter of fact, it is rather common to see the PLC instabilities change during a tensile strength test, and to encounter type A, then type B and finally type C bands [33]. This is exactly what happened during our tensile strength tests. However, what is more unexpected is that the instabilities are different depending on the configuration. We can note that the PLC instabilities are relatively identical in configurations No. 1 and No. 2, but quite different in configuration No. 3, where the frequency is higher. We can observe that, in the Z direction, the PLC instabilities do not appear to be modified. For example, we obtained a frequency of 1.53 Hz ± 0.16 Hz and an amplitude of 2.28 MPa ± 0.41 MPa for the 5% elongation, and a frequency of 0.63 Hz ± 0.06 Hz and an amplitude of 3.86 MPa ± 0.41 MPa for the 15% elongation in the case of configuration No. 3, which is close to the values presented in Table 6.

Study of the structure – metallurgical examinations

Figure 7 shows, at low magnification, after electrolytic etching and under polarised light, the granular structure of the 3 configurations studied, in the as-fabricated state. We can see that the deposited weld beads consist of columnar grains in the central zone (core structure), and that a fine-grained zone develops at the interface between two weld beads. Configuration No. 3 (see Figure 7c) is a perfect illustration of this structure. The columnar grains are oriented according to the temperature gradient during solidification, i.e. the grains tend to develop along trajectories orthogonal to the isotherms, which is in line with the laws of solidification [33]. In conventional welding, crystallisation of the metal during solidification is epitaxial, whereby the crystals of the solid metal being formed (in this case, 5356 aluminium alloy) adopt the same orientation as the crystals of the base metal on which they rest [33] and develop in a columnar manner. However, as indicated above, this is not what we observe here, given the presence of a fine-grained zone between each deposited weld bead (see Figure 8a for the detail). The observations made using optical microscopy (not shown) indicate no modification of the structure after the heat treatment of 1.5 h at 350 °C. There is neither grain growth nor recrystallisation.

As previously mentioned, the fine-grained zone phenomenon is more pronounced for configuration No. 3, where this zone can extend to a width of 500 µm; we can assume that this is related to the welding synergy. To go further, we are continuing our study on configuration No. 3. Figure 8b shows a higher concentration of constituents (intermetallic compounds, dispersoids, precipitates) in the fine-grained zones than in the centre of the weld beads (columnar-grained zone). An EDS study (see Figure 9) allowed us to identify the constituents, namely:

- Presence of Mg_2Si. This phase has extremely reduced solubility, which means that it can typically be observed outside a solid solution, even with a low Si content [34].
- Presence of Si and O in dark areas of the FEG-SEM image (Figure 9). In fact, this is SiO_2 (colloidal silica) which was used to polish

Table 6. Frequencies and amplitudes of the PLC instabilities depending on the fabrication configuration

Configuration	1		2		3	
Strain	5%	15%	5%	15%	5%	15%
Frequency (in Hz)	0.71 ± 0.08	0.44 ± 0.05	0.65 ± 0.08	0.30 ± 0.04	1.48 ± 0.25	0.63 ± 0.05
Amplitude (in MPa)	2.51 ± 0.38	3.89 ± 0.57	1.95 ± 0.32	3.93 ± 0.57	2.49 ± 0.28	4.08 ± 0.42
Example of measurement on conf. No. 3 at 5% strain.	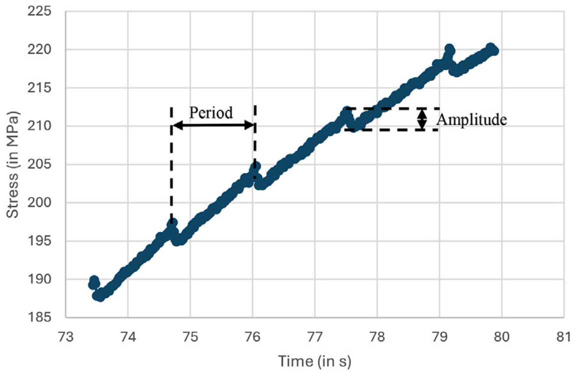					

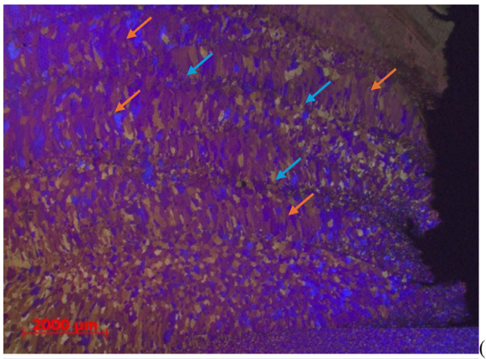

(a) Configuration No. 1

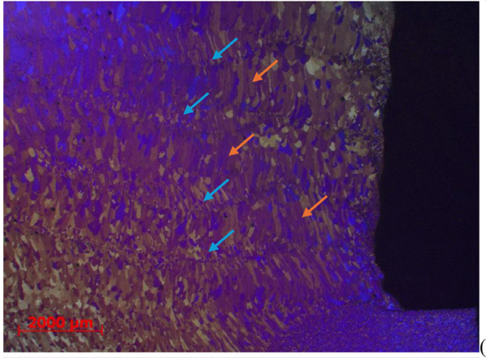

(b) Configuration No. 2

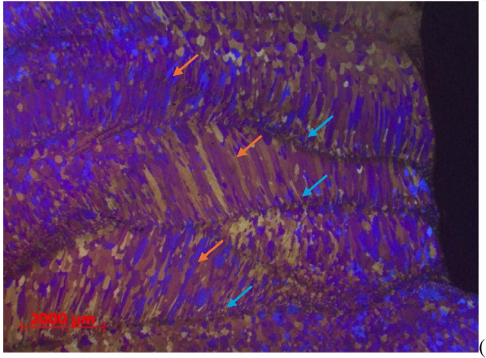

(c) Configuration No. 3

Figure 7. Metallurgical examinations – magnification 12x, as built: orange arrows – columnar grained zone, blue arrows – fine-grained zone

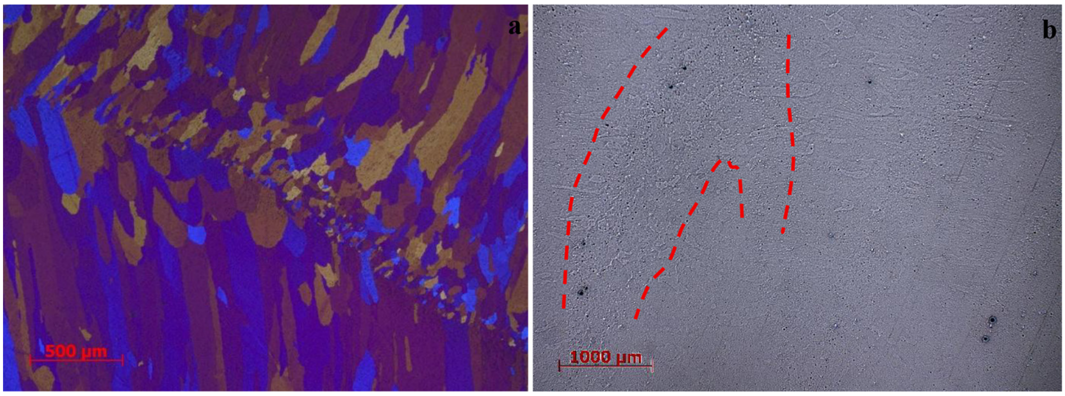

Figure 8. Example of configuration No. 3, as built: (a) detail of a fine-grained zone at the interface between two beads, (b) example of concentration of constituents: area delineated by a red dotted line

the samples and remained trapped in shrinkage cavities: micro-shrinkage cavities (item 1, Figure 9) or gas pores (item 2, Figure 9). Round-shaped gas pores (Table 4) result from the presence of hydrogen which is dissolved in the liquid aluminium and forms bubbles during solidification. The micro-shrinkage cavities have more tortuous shapes and stem from volume contraction during cooling [35].

- Presence of many compounds containing Fe. Fe is never associated with Si, but it sometimes combines with Cr and Mn (Figure 9), thus forming Al_6(Fe, Mn, Cr) in particular [34, 36].
- Compounds containing Cr and/or Mn, but not containing Fe, and which may be Al_7Cr and Al_6(Mn, Cr) [34].

In addition, the Mg distribution resulted in the formation of dendrites within the grains (Figure 9 and Figure 10). Mg is present in significant amounts in solid solution in the alloy but, as it contents increases, it appears in the Al_3Mg_2 eutectic form. When the Mg content exceeds approximately 3.5%, Al_3Mg_2 can precipitate at the grain boundaries or inside the grains [34]. Note that after heat treatment (1.5 hours at 350 °C), the dendrites "fade away" (although not completely); this is very probably due to Mg being better homogenised in the solid solution.

The fine-grained zones originate from precipitation of the constituents at the edge of the weld beads, causing more abundant nucleation. This precipitation is probably due to a change in the temperature gradients and in the cooling rate, which is related to the welding strategy. Configuration No. 3 has a lower linear welding energy than the other two configurations; this can explain these more pronounced fine-grained zones. In addition, this phenomenon can be associated with selective growth, where grains whose preferred growth direction coincides with the solidification trajectory result more developed at the expense of the neighbouring grains [33]. This entails the disappearance of the least favourably oriented grains, leading to a decrease in the number of grains and, therefore, an increase in their size and columnar growth.

Relationship between microstructure and mechanical properties

In view of the characterisations previously carried out, we are now in a position to analyse the relationships between the microstructure and the mechanical properties, i.e. establish a correlation between the mechanical behaviour and the microstructure. In the remaining part of this study, we will take the example of configuration No. 3 in the as built condition.

The idea [37] is based on the possibility of calculating the various contributions of the microstructure to the hardening mechanisms of 5356 aluminium alloy in the as built condition, and more specifically, to the yield strength. The hardening mechanisms identified are listed below:

- Grain size refinement: this is the Hall-Petch equation.
- Solid solution, with introduction of foreign atoms into the matrix, causing distortions in the crystal lattice.
- Precipitation, resulting in precipitates being placed on the pathway of the dislocations, thereby preventing dislocation motion.
- Strain hardening, which is related to the density of dislocations present in the alloy.

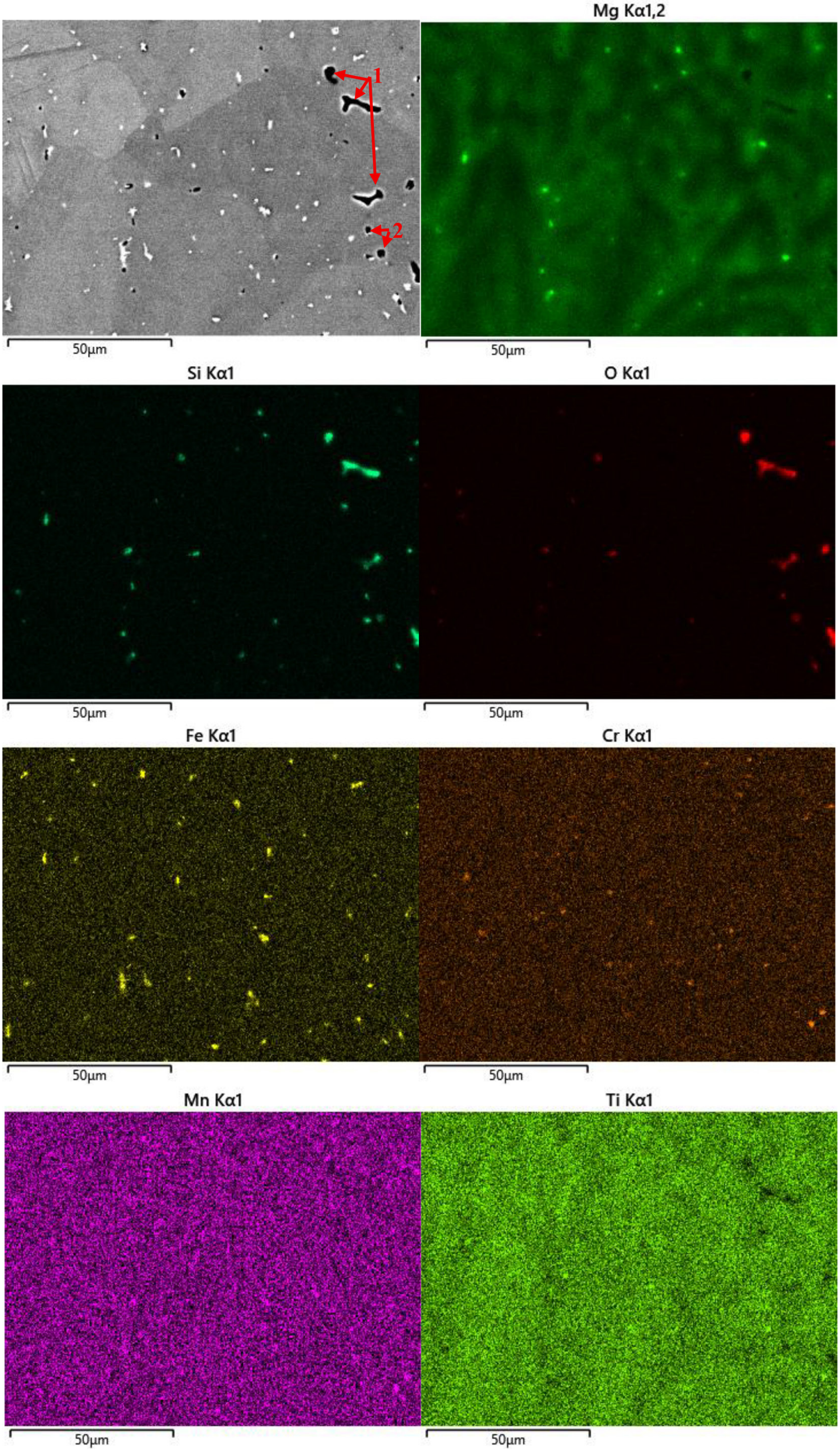

Figure 9. Configuration No. 3, as built – EDS analysis

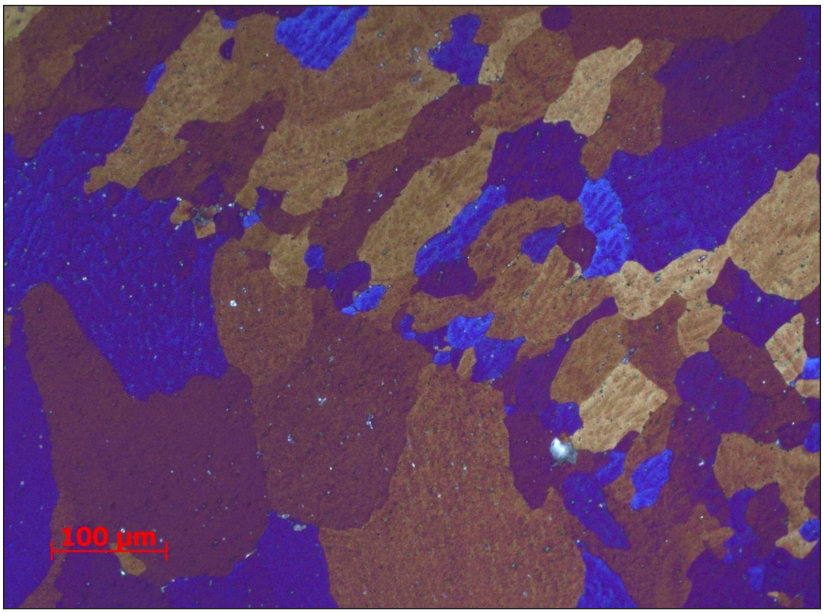

Figure 10. Configuration No. 3, as built – optical microscope observation of the dendrites after Barker etching

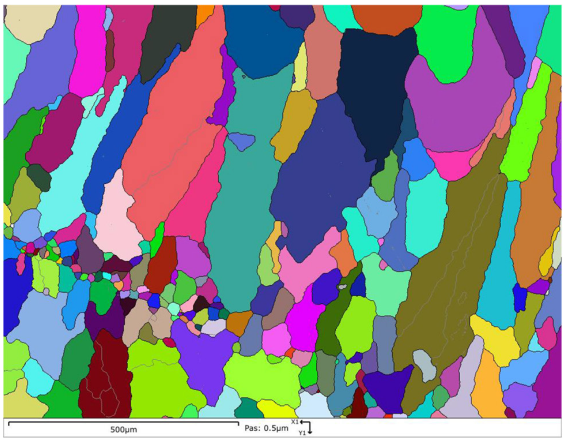

Threshold angle: 10°

Grain size number as per standard ASTM E2627: 4.8

Mean equivalent circle diameter: 56.3 µm

Figure 11. EBSD observation on a sample from configuration No. 3 in the as built condition. Grain map (in random colours) and grain boundaries (threshold angle 10°)

Contribution of grain size to the yield strength

As previously mentioned, the relationship which connects the grain size and the yield strength (σ_e is the Hall-Petch equation [38]:

$$\sigma_{eGB} = \sigma_0 + \frac{k}{\sqrt{d}} \tag{3}$$

where: σ_{eGB} is the contribution of grain refinement strengthening to the yield strength; σ_0 is the friction stress; k is the Hall-Petch slope; and d is the average grain diameter.

For aluminium alloys, σ_0 = 13 MPa and k = 2.3 MPa $\sqrt{mm}$ [38]. The experimental parameter that needs to be determined is the average grain diameter (i.e. the grain size). The average value of d is 56.3 µm, given by Figure 11. This gives: σ_{eGB} = 22.7 MPa.

Contribution of structural hardening to the yield strength

The only hardening precipitate present in the alloy is Mg_2Si (see above). Furthermore, Si only participates in the formation of this precipitate (refer to paragraph "Study of the structure – metallurgical examinations"). Given that there is very little Si (% by mass) available in the alloy, the $\%Mg_2Si$ (% by mass) available for hardening can be calculated as follows:

$$\%Mg_2Si \text{ (by mass)} = 2.729 \text{ x } \%Si \text{ (by mass), when Mg is in excess} \tag{4}$$

Considering 0.07% Si (Table 3), this gives 0.19% Mg_2Si (by mass) available for hardening, which corresponds to approximately 35 MPa using the chart available in [36]. Hence σ_{ep} (Contribution of structural hardening to the yield strength) = 35 MPa.

Contribution of solid solution to the yield strength

The effect of solid solution hardening on the yield strength was studied by Myhr et al [39] and can be defined as follows:

$$\sigma_{ess} = \sum_i K_i\, C_i^{\frac{2}{3}} \tag{5}$$

where: σ_{ess} is the contribution of solid solution hardening to the yield strength; C_i is the concentration of element i in the alloy, expressed in % by mass; and K_i s a hardening constant related to element i.

In our case, K_{Mg} = 18.6 MPa [34]. The experimental parameter that needs to be determined is the concentration of element Mg (% by mass). Since Mg is either in solid solution or used in Mg_2Si, we just need to determine the quantity consumed by Mg_2Si, i.e. 0.12% (by mass) according to the previous paragraph. Therefore, there is 4.64% Mg (by mass) in the solid solution. This gives σ_{ess} = 51.7 MPa.

Contribution of strain hardening or dislocations to the yield strength

In this case, the corresponding strain hardening in the yield strength can be estimated with the Bailey-Hirsch relationship [40]:

$$\sigma_{edis} = M\chi\, \mu b \sqrt{\rho} \tag{6}$$

where: σ_{edis} is the contribution of strain hardening to the yield strength; M is the Taylor factor; χ is a constant related to the material; μ is the shear modulus; b is the Burgers vector; and ρ is the dislocation density.

For aluminium alloys, $M = 3.06$, $\mu = 26.9$ GPa, $b = 0.286$ nm, $\chi = 0.27$ [41]. The experimental parameter that needs to be determined is the dislocation density, i.e. the ρ_{GND} value measured (as an example) in Figure 12 at $0.38.10^{14}$ /m² (average density). This gives σ_{edis} = 39.2 MPa.

The EBSD technique only allows the density of geometrically necessary dislocations (GND) to be obtained and does not provide information on the total dislocation density, which consists of the density of geometrically necessary dislocations and the density of statistically stored dislocations. It should be noted that we considered σ_{edis} to be essentially due to ρ_{GND}. For the first moments of plastic yielding or for the end of elasticity (yield point zone), the contribution of ρ_{GND} to strain hardening is the most significant [42].

Total contribution to the yield strength and analyses

There are various ways of adding together the contributions to the yield strength, especially when obstacles of identical strength but different densities are present. In this case, we use the Deschamps model [43]:

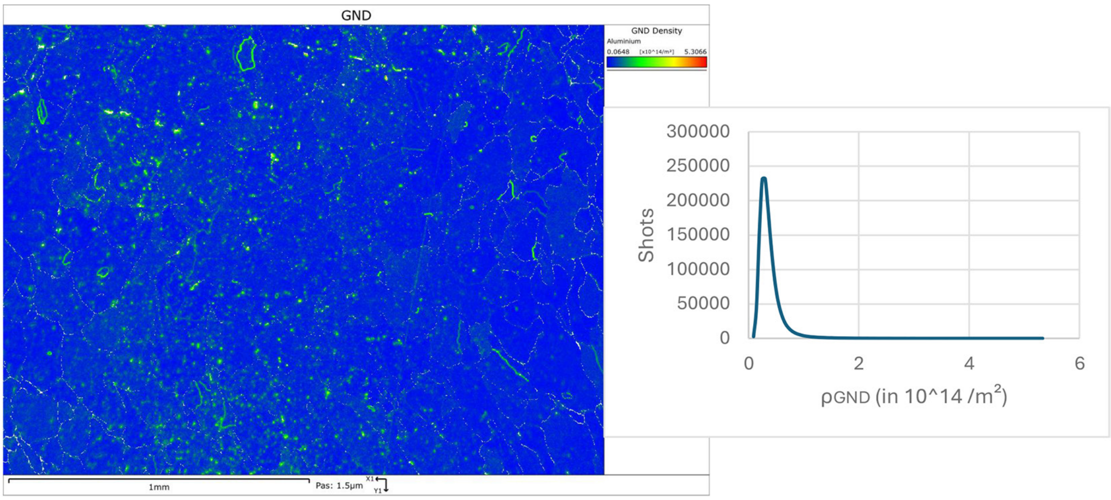

Figure 12. Density of geometrically necessary dislocations (ρ_{GND}) from EBSD observations. Configuration No. 3, as built

$$\sigma_{etotal} = \sigma_{eGB} + \sigma_{ess} + \sqrt{\sigma_{ep}^2 + \sigma_{edis}^2} \quad (7)$$

This gives σ_{etotal} = 127 MPa, a value which can be compared to the average $Rp_{0.2}$ in the as-fabricated state (see Figure 5), which is 118 MPa.

A difference of around 7.5% can be noted between the two values. This can be explained in many ways, but in particular by the value of σ_{ep} which is between 0 MPa and 35 MPa. In fact, a significant portion of the Mg_2Si is present in the alloy in the form of constituents that are not coherent with the matrix, i.e. β-Mg_2Si which does not contribute to hardening, and not in the form of β'' or β' hardening precipitates. If all of the available Mg_2Si (0.19% by mass) actually contributed to hardening, then σ_{ep} would be equal to a maximum of 35 MPa [36]. This is not the case. Taking (for example) σ_{ep} = 17.5 MPa, we obtain σ_{etotal} = 117 MPa, to be compared to 118 MPa.

CONCLUSIONS

This study highlights the relevance of an approach that combines designs of experiments and artificial neural networks for optimising the parameters of the WAAM process applied to 5356 aluminium alloy. The morphological analysis of the optimised structures revealed several key points:

- The CMT MIG welding synergy allows stable building without sagging of the edges (unlike what occurs with mixed CMT and pulsed MIG welding).
- Fine adjustment of the parameters is necessary for the first layers, in particular in CMT MIG welding, in order to achieve improved penetration.
- The width of the walls and the penetration into the substrate increase linearly as the linear welding energy increases, while the layer thickness decreases.

The three optimized configurations exhibit comparable material integrity with very few defects: all configurations show a porosity rate below 0.2%.

The hardness measurements showed good homogeneity of the test specimens and the three configurations, both in the as-fabricated state and after annealing treatment. The results of the electrical conductivity measurements confirmed these observations, suggesting microstructural stability after heat treatment.

The tensile tests carried out in the as built condition revealed the following:

- Similar mechanical properties between the three configurations.
- Performance in line with data from the literature.
- High mechanical strength (250 MPa to 270 MPa), along with good elongation (25% to 30%).
- Moderate anisotropy between the building direction and the longitudinal direction of the test specimens.
- Presence of Portevin–Le Chatelier instabilities, typical of the 5000 series aluminium alloys.

The microstructural analysis, particularly for configuration No. 3, revealed the presence of columnar grains in the core structure of the weld beads, along with fine-grained interfacial zones. The latter are a consequence of increased nucleation, induced by a high concentration of constituents, dispersoids and precipitates, as well as selective grain growth. The phases identified, namely Mg_2Si, Al_6(Fe, Mn, Cr), Al_7Cr, and Al_6(Mn, Cr), are typical of the 5356 aluminium alloy. The microstructure is also characterised by the presence of gas pores caused by hydrogen, along with micro-shrinkage cavities. We also noted the presence of dendrites highlighted by the Al_3Mg_2 eutectic.

Lastly, we established a correlation between the microstructure and the mechanical properties by breaking down the four hardening mechanisms, highlighting a consistent match between structural characteristics and mechanical performance.

Acknowledgements

The authors wish to thank CETIM (Centre Technique des Industries de la Mécanique – Technical Centre for the mechanical industries) for the funding and support provided for this study.

REFERENCES

1. Çam G. Prospects of producing aluminum parts by wire arc additive manufacturing (WAAM). Materials Today: Proceedings. 2022;62:77–85. http://dx.doi.org/10.1016/j.matpr.2022.02.137

2. Wang Y, Chen X, Konovalov SV. Additive manufacturing based on welding arc: A low-cost method. Journal of Surface Investigation: X-ray, Synchrotron and Neutron Techniques. 2017 Nov;11(6):1317–28. http://dx.doi.org/10.1134/s1027451017060210
3. Williams SW, Martina F, Addison AC, Ding J, Pardal G, Colegrove P. Wire + arc additive manufacturing. Materials Science and Technology. 2016 May;32(7):641–7. http://dx.doi.org/10.1179/1743284715y.0000000073
4. Patel M, Mulgaonkar S, Desai H, Borse T. Development and implementation of wire arc additive manufacturing (WAAM) based on pulse spray GMAW for aluminum alloy (AlSi7Mg). Transactions of the Indian Institute of Metals. 2021 Jan 22;74(5):1129–40. http://dx.doi.org/10.1007/s12666-020-02154-w
5. Tawfik MM, Nemat-Alla MM, Dewidar MM. Enhancing the properties of aluminum alloys fabricated using wire + arc additive manufacturing technique - A review. Journal of Materials Research and Technology. 2021 Jul;13:754–68. http://dx.doi.org/10.1016/j.jmrt.2021.04.076
6. Cong B, Ding J, Williams S. Effect of arc mode in cold metal transfer process on porosity of additively manufactured Al-6.3%Cu alloy. The International Journal of Advanced Manufacturing Technology. 2014 Sep 23;76(9–12):1593–606. http://dx.doi.org/10.1007/s00170-014-6346-x
7. Ding D, Pan Z, Cuiuri D, Li H. Wire-feed additive manufacturing of metal components: technologies, developments and future interests. The International Journal of Advanced Manufacturing Technology. 2015 May 9;81(1–4):465–81. http://dx.doi.org/10.1007/s00170-015-7077-3
8. Hu Z, Xu P, Pang C, Liu Q, Li S, Li J. Microstructure and mechanical properties of a high-ductility Al-Zn-Mg-Cu aluminum alloy fabricated by wire and arc additive manufacturing. Journal of Materials Engineering and Performance. 2022 Feb 23;31(8):6459–72. http://dx.doi.org/10.1007/s11665-022-06715-6
9. Vishnukumar M, Pramod R, Rajesh Kannan A. Wire arc additive manufacturing for repairing aluminium structures in marine applications. Materials Letters. 2021 Sep;299:130112. http://dx.doi.org/10.1016/j.matlet.2021.130112
10. Péchiney Rhenalu. Aluminum semi-finished products. 1st ed. Paris: Péchiney-Rhenalu; 1997. (in French).
11. Wieczorowski M, Pereira A, Carou D, Gapinski B, Ramírez I. Characterization of 5356 aluminum walls produced by wire arc additive manufacturing (WAAM). Materials. 2023 Mar 23;16(7):2570. http://dx.doi.org/10.3390/ma16072570
12. Zhu K, Wang J, Zhang W Chen, Zhu X Lei, Lu X Feng. Effect of deposition strategies on microstructures, defects and mechanical properties of 5356 aluminum alloy by wire arc additive manufacturing. Transactions of Nonferrous Metals Society of China. 2024 Feb;34(2):423–34. http://dx.doi.org/10.1016/s1003-6326(23)66408-8
13. Köhler M, Hensel J, Dilger K. Effects of thermal cycling on wire and arc additive manufacturing of Al-5356 components. Metals. 2020 Jul 15;10(7):952. http://dx.doi.org/10.3390/met10070952
14. Jiangang P, Bo Y, Jinguo G, Yu R, Hongjun C, Liang Z, et al. Influence of arc mode on the microstructure and mechanical properties of 5356 aluminum alloy fabricated by wire arc additive manufacturing. Journal of Materials Research and Technology. 2022 Sep;20:1893–907. http://dx.doi.org/10.1016/j.jmrt.2022.08.005
15. Develay R. Wrought aluminium and aluminium alloys: metallic properties. Study and properties of metals. 1992 Apr. http://dx.doi.org/10.51257/a-v1-m438. (in French).
16. Vargel C. Aluminium metallurgy. Study and Properties of Metals. 2010 Mar. http://dx.doi.org/10.51257/a-v1-m4663 (in French).
17. Mauduit A, Pillot S, Frascati F. Application study of AlSi10Mg alloy by selective laser melting: physical and mechanical properties, microstructure, heat treatments and manufacturing of aluminium metallic matrix composite (MMC). Metallurgical Research & Technology. 2015;112(6):605. http://dx.doi.org/10.1051/metal/2015039
18. Spierings AB, Schneider M, Eggenberger R. Comparison of density measurement techniques for additive manufactured metallic parts. Rapid Prototyping Journal. 2011 Aug 2;17(5):380–6. http://dx.doi.org/10.1108/13552541111156504
19. Cong B, Ouyang R, Qi B, Ding J. Influence of cold metal transfer process and its heat input on weld bead geometry and porosity of aluminum-copper alloy welds. Rare Metal Materials and Engineering. 2016 Mar;45(3):606–11. http://dx.doi.org/10.1016/s1875-5372(16)30080-7
20. Derekar KS. A review of wire arc additive manufacturing and advances in wire arc additive manufacturing of aluminium. Materials Science and Technology. 2018 May;34(8):895–916. http://dx.doi.org/10.1080/02670836.2018.1455012
21. Robert P. Design and manufacturing of metallic smart parts with WAAM technology [PhD thesis]. Grenoble (France): Université Grenoble Alpes; 2022. (in French).
22. Box GEP, Behnken DW. Some new three level designs for the study of quantitative variables. Technometrics. 1960 Nov;2(4):455–75. http://dx.doi.org/10.1080/00401706.1960.10489912
23. Cybenko G. Approximation by superpositions of a sigmoidal function. Mathematics of Control, Signals, and Systems. 1989 Dec;2(4):303–14. http://dx.doi.org/10.1007/bf02551274

24. Hornik K. Approximation capabilities of multilayer feedforward networks. Neural Networks. 1991;4(2):251–7. http://dx.doi.org/10.1016/0893-6080(91)90009-t
25. Rumelhart DE, Hinton GE, Willians RJ. Learning internal representations by error propagation. Readings in Cognitive Science. 1988;399–421. http://dx.doi.org/10.1016/b978-1-4832-1446-7.50035-2
26. Prechelt L. Automatic early stopping using cross validation: quantifying the criteria. Neural Network. 1998 Jun;11(4):761–7. http://dx.doi.org/10.1016/s0893-6080(98)00010-0
27. Geng H, Li J, Xiong J, Lin X, Zhang F. Geometric limitation and tensile properties of wire and arc additive manufacturing 5A06 aluminum alloy parts. Journal of Materials Engineering and Performance. 2016 Dec 22;26(2):621–9. http://dx.doi.org/10.1007/s11665-016-2480-y
28. Yehorov Y, da Silva LJ, Scotti A. Balancing WAAM production costs and wall surface quality through parameter selection: A case study of an Al-Mg5 alloy multilayer-non-oscillated single pass wall. Journal of Manufacturing and Materials Processing. 2019 Apr 16;3(2):32. http://dx.doi.org/10.3390/jmmp3020032
29. Quérard V. Manufacturing of large-scale aeronautical parts by WAAM additive manufacturing [PhD thesis]. Nantes (France): École Centrale de Nantes; 2019. (in French).
30. Boeira AP, Ferreira IL, Garcia A. Alloy composition and metal/Mold heat transfer efficiency affecting inverse segregation and porosity of as-cast Al–Cu alloys. Materials & Design. 2009 Jun;30(6):2090–8. http://dx.doi.org/10.1016/j.matdes.2008.08.032
31. Gu JL, Ding JL, Cong BQ, Bai J, Gu HM, Williams SW, et al. The influence of wire properties on the quality and performance of Wire+Arc additive manufactured aluminium parts. Advanced Materials Research. 2014 Dec;1081:210–4. http://dx.doi.org/10.4028/www.scientific.net/amr.1081.210
32. Portevin A, Le Chatelier F. On the plastic instability of alloys. C R Acad Sci Paris. 1923;176:507. (in French).
33. Granjon H. Metallurgical fundamentals of welding. Paris: Publications de la Soudure Autogène; 1989. (in French).
34. Davis JR, editor. Aluminum and aluminum alloys. Materials Park (OH): ASM International; 1993.
35. Imširović M, Trdan U, Klobčar D, Bračun D, Nagode A, Berthe L. Mitigating defects in directed energy deposited aluminium 5356 alloy through in-situ workpiece vibration. Journal of Materials Research and Technology. 2024 Nov;33:1581–99. http://dx.doi.org/10.1016/j.jmrt.2024.09.179
36. Totten GE, MacKenzie DS, editors. Handbook of Aluminum. CRC Press; 2003. http://dx.doi.org/10.1201/9780203912591
37. Mauduit A, Salesse L, Bachelard N, Gransac H. A study of nanostructured 7034 aluminium alloy: Relationship between microstructure and mechanical properties. Annales de Chimie - Science des Matériaux. 2025 Jun 30;49(3):219–33. http://dx.doi.org/10.18280/acsm.490301
38. Armstrong RW. 60 years of hall-Petch: past to present nano-scale connections. Materials Transactions. 2014;55(1):2–12. http://dx.doi.org/10.2320/matertrans.ma201302
39. Myhr O. Modelling of the age hardening behaviour of Al–Mg–Si alloys. Acta Materialia. 2001 Jan;49(1):65–75. http://dx.doi.org/10.1016/s1359-6454(00)00301-3
40. Bailey JE, Hirsch PB. The dislocation distribution, flow stress, and stored energy in cold-worked polycrystalline silver. Philosophical Magazine. 1960 May;5(53):485–97. http://dx.doi.org/10.1080/14786436008238300
41. Basinski SJ, Basinski ZS. Dislocations in solids. Amsterdam: North-Holland Publishing Co.; 1979.
42. Rudloff M. Study of volume/surface transition mechanisms in the mechanical behavior of a Ni20Cr alloy [PhD thesis]. Compiègne (France): Université de Technologie de Compiègne; 2010. (in French).
43. Deschamps A, Brechet Y. Influence of predeformation and ageing of an Al–Zn–Mg alloy—II. Modeling of precipitation kinetics and yield stress. Acta Materialia. 1998 Dec;47(1):293–305. http://dx.doi.org/10.1016/s1359-6454(98)00296-1